Research paper

Ground view factor computation model for bifacial photovoltaic collector field: uniform and non-uniform surfaces

Marzia Alam [a],*, Mehreen Saleem Gul [a], Tariq Muneer [b]

[a] *School of Energy, Geoscience, Infrastructure and Society (EGIS), Heriot-Watt University, Riccarton Campus, Edinburgh, EH14 4AS, UK*
[b] *School of Engineering and Built Environment, Edinburgh Napier University, 10 Colinton Rd, Edinburgh, EH10 5DT, UK*

ARTICLE INFO

ABSTRACT

The photovoltaic collectors in a field are subject to three types of solar radiation: direct, diffuse, and reflected irradiance. The reflected irradiance received by solar photovoltaic (PV) depends on the view factor from solar PV to the ground. This view factor component is dominant for bifacial PV due to additional reflected irradiance gain, which can be achieved from the module's rear side.

This paper proposes and verifies a finite element method based view factor computation model, which can handle both uniform and non-uniform ground surfaces. The unique contribution of this work is that it introduces a geometric progression based finite element mesh generation process that forms the quasi-uniform grid. The generated grid values are fitted into the computation model to calculate the view factor from bifacial photovoltaics to the ground, known as the ground view factor (GVF). The proposed computation model can achieve an accuracy of 99%. To keep accuracy at this level, the smallest element size of the coarse mesh should be within 0.1%–0.4% of surface width or length. Moreover, the geometric progression ratio of the fine and coarse mesh should be in the range of 1.001–1.002 and 1.01–1.04, respectively. The model is analysed under six different PV field variables: multiple reflective ground surfaces, the height of PV, tilted ground surface, PV position in the ground, length and width of the ground, and PV string length. For the different string sizes considered here, the view factor model's computation time varies from 180 s to 257 min for the iteration size of 7.67 billion to 765 billion. The view factor computation model will contribute to analyse reflected irradiance at the rear side of bifacial PV, which is essential to predict the energy generation accurately. The proposed model is also beneficial for urban planning and addressing heat gain of the building-integrated PV system and energy usage.

1. Introduction

An inclined photovoltaic (PV) panel receives three types of solar radiation: direct, diffuse and reflected radiation. For traditional monofacial panels, the reflected irradiation component constitutes around 10% maximum of the total incident radiation (Mckay, 1985). This, however, differs in the case of the latest bifacial PV, where increased output can be achieved due to the rear side being able to receive significant irradiance gain from the ground reflected radiation component (Guerrero-Lemus et al., 2016). The reflected irradiation relies on the view factor from solar PV to the ground, known as the ground view factor (GVF). This work focuses explicitly on the view factor of bifacial PV, which is a geometry dependent parameter. It is a ratio that defines the fraction of energy, leaving an opaque, isothermal,

and diffuse surface that directly strikes upon another surface. Different methods are available to compute view factors such as cross-strings, double area integration, unit sphere methods, and monte Carlo methods (Gupta et al., 2017; Francisco et al., 2014; Howell et al., 2020). This work applies the double area integration method to calculate the ground view factor (GVF) from solar PV to the ground.

To understand the concept of view factor, let us assume two surfaces A_1 and A_2, where r is the distance between two differential elements dA_1 and dA_2 of the respective surfaces (Fig. 1). The angles between normal to each surface: n_1 and n_2 with the line 'r' are given as Φ_1 and Φ_2, respectively. Therefore, the view factor between surface A_1 and A_2 is:

$$F_{A_1-A_2} = \frac{1}{A_1} \iint_{A_1 A_2} \frac{cos\varnothing_1 cos\varnothing_2}{\pi r^2} dA_1 dA_2 \tag{1}$$

If A_1 and A_2 surfaces have dimension ($length \times width$), $b \times a$ and $d \times c$ respectively $\varnothing$ is the angle between the surfaces A_1 and A_2 and $\varnothing = \pi - \beta$, then Eq. (1) can be derived as Muneer et al.

List of abbreviations

Photovoltaic (PV)
Geometric progression (GP)
Ground view factor (GVF)
View factor (VF)
Partial differential equation (PDE)
Finite element method (FEM)
Grading factor (GF)
Integrated development environment (IDE).
Just-in-time (JIT)
Low level virtual machine (LLVM)
Application program interface (API)
Ordinary least square regression (OLS)
Central processing unit (CPU)
Ground clearance height (GCH)

List of units

View factor, VF — no unit
Rate of convergence, β: — no unit
Reflectivity, ρ: — no unit
Tilt angle, Φ: — degree (°)
Irradiance, I_T: — (W/m^2)
Length and width (x, y) : — metre (m)
Ground clearance height (GCH): — metre (m)
Area, A: — metre (m^2)
Time, t: — second (s)/minute (min)
Voltage, V: — Volt (V)

Fig. 1. View factor between two surfaces A_1 and A_2 (Howell et al., 2020).
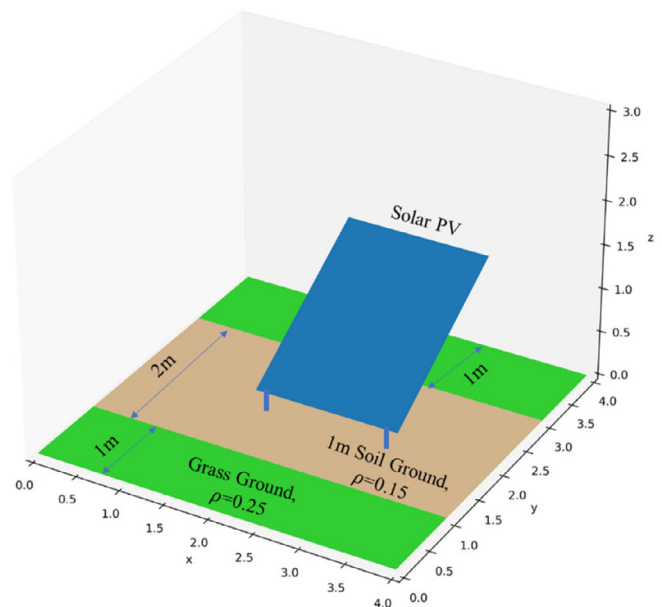
Fig. 2. Bifacial PV in a uniform ground covered by grass and soil reflective surface.

(2015),

$$F_{A_1-A_2} = \frac{1}{ab} \int_{y_1=0}^{a} \int_{x_1=0}^{b} \int_{y_2=0}^{c}$$

$$\times \int_{x_2=0}^{d} \frac{y_1 y_2 \sin^2 \beta}{\pi \left[y_1^2 + y_2^2 + 2y_1 y_2 \cos\beta + (x_1 - x_2)^2 \right]^2} dx_2 dy_2 dx_1 dy_1$$

(2)

Here, β is the acute (if $\Phi > 90°$) or the obtuse angle (if $\Phi < 90°$) between two surfaces A_1 and A_2. x_1, x_2, represents the coordinates of lengths and y_1, y_2 represents the coordinates of the width of the A_1 and A_2 surfaces, respectively. The words, 'length' and 'width' can be used alternatively depending on the surface orientation. The surface can either be in landscape or portrait orientation. The term 'a' and 'c' in Eq. (2) refer to the Y-axis coordinates whether 'a' and 'c' are length or width. Similarly, the term 'b' and 'd' refer to the X-axis co-ordinates. However, for the surfaces with equal dimensions, length and width are the same.

The computation of the view factor for the uniform ground surface is relatively straightforward and easily solvable by simple numerical integration methods such as midpoint rule, Simpson rule, and trapezoidal rule (Arthur et al., 1986). The term 'uniform ground' means a homogeneous surface that has a consistent specific terrain. The spatial pattern of the surface is homogeneous in texture, structure, and composition. In a solar PV field, a uniform ground indicates a ground field with flat terrain and is composed of one or more ground reflective surfaces in a regular pattern, as shown in Fig. 2. The figure shows that the foreground area of AB = 1 m is composed of grass surface with reflectivity, $\rho = 0.25$, followed by BC = 2 m of the soil surface with reflectivity $\rho = 0.15$ and CD = 1 m grass surface again at the rear side of the bifacial PV.

However, challenges arise in dealing with the non-uniform ground where the straightforward numerical integration method cannot be applied due to the irregular pattern of non-uniform surfaces. An example of a non-uniform ground is a PV field comprising of grass ($\rho = 0.25$), soil ($\rho = 0.15$), and brick surfaces ($\rho = 0.20$) in a random pattern (Fig. 3) that causes the incident irradiance's inhomogeneity at the rear side. Due to this inhomogeneity, the meshing of both the PV and the ground surface is essential (Libal and Kopecek, 2018).

To date, there have been various research studies on sky view factor computation. For example, the sky view factor (SVF) for urban heat island studies is calculated in Dirksen et al. (2019). There have been urban planning studies where novel methods were developed for sky view factor computation (Rehman and Siddiqui, 2015). An image processing based sky view factor computation approach for urban climate modelling is shown in Middel et al. (2018), which applies the annulus method. However, there
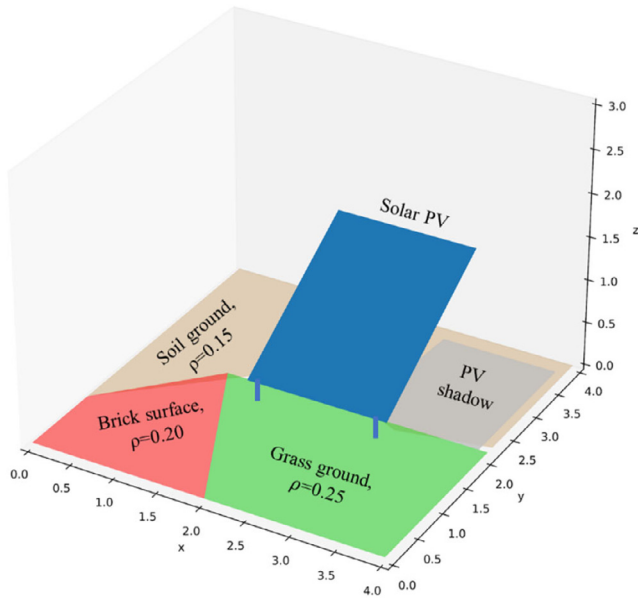
Fig. 3. Bifacial PV in a non-uniform ground covered by grass, soil and brick reflective surface.

has been limited published work on ground view factor computation specific to the bifacial solar PV to date. An analytical expression was developed to compute view factor of flat solar collectors (Fathi and Samer, 2016). A Monte Carlo based method is applied to calculate the view factor between solar chimney power plant and solar tower (Mirhosseini et al., 2017). A remarkable contribution has been made by Applebaum on view factor computation using the cross-string methods. However, these methods are limited to the mathematical expression only (Appelbaum and Aronescu, 2016; Appelbaum, 2016, 2018). There are few irradiances computation models, such as bifacialvf and pvfactors (Asgharzadeh et al., 2019), which have been developed based on the concept of view factor. The model 'bifacialvf' uses the angle of incident (AOI) correction method to compute view factor, and the pvfactors model uses the analytical solution of view factor to determine irradiance received by the front and rear side of the module. These models are 2D models and consider infinite lengths of module rows, whereas our view factor computation model is 3D, which assumes the finite length of module rows and the module's width and heights can be varied. The authors of this paper, Muneer et al. (Muneer et al., 2015), developed a finite element method based view factor computation model in Microsoft Excel Visual Basic environment (VBA). Further to this work, Alam et al. developed a uniform grid-based view factor computation model in Python (Alam et al., 2019) to reduce the computation time incurred in VBA due to increasing the number of elements of the uniform grid. This paper expands on the previous work and proposes a geometric progression-based quasi-uniform mesh generation method where the grids are nearly uniform. The proposed finite element mesh generation method divides the solar PV and the ground reflecting surface into several meshes/grids and thereby apply Eq. (2) to compute the view factor from solar PV to ground. Specifically, this work is focused on view factor computation for the bifacial PV module's rear side, which is prone to nonhomogeneous reflected irradiance. One of the causes of non-uniformity is the presence of shadows on the ground. Therefore, it requires calculating view factor to shaded and non-shaded ground surface separately, which has been discussed in paper (Alam et al., 2021). In this paper, the sensitivity of the view factor is tested under various PV field scenarios such as module

deployment height, multiple reflective ground surfaces, inclined ground surface, module position in the ground, length and width of the ground and different PV string lengths.

The paper organisation is as follows. Section 2 describes the view factor in the context of the solar PV field. The methodology of finite element mesh generation for the view factor simulation framework is introduced in Section 3. Section 4 presents the view factor computation results and analysis for various PV field scenarios. Finally, Section 5 provides some concluding remarks.

2. View factor for solar PV collector

To understand the implication of the view factor in a solar PV field, let us consider a tilted solar PV collector(c) of an area A_c. The total incident radiation on the PV surface consists of direct, diffuse and reflected radiation and can be written as (Duffie and Beckman, 2013),

$$A_c I_T = I_b R_b A_c + I_{d,iso} A_s F_{s-c} + I_{d,cs} R_b A_c + I_{d,hz} A_{hz} F_{hz-c}$$
$$+ \sum_n I_n \rho_n A_n F_{n-c} \tag{3}$$

By using the reciprocity theorem of view factor it can be written,

$$A_n F_{n-c} = A_c F_{c-n}; A_s F_{s-c} = A_c F_{c-s}; A_c F_{c-hz} = A_{hz} F_{hz-c} \tag{4}$$

Eq. (3) can therefore be re-written as,

$$I_T = I_b R_b + I_{d,iso} F_{c-s} + I_{d,cs} R_b + I_{d,hz} F_{c-hz} + \sum_n I_n \rho_n F_{c-n} \tag{5}$$

In Eq. (3), $I_b R_b$ is the beam contribution on the PV collector c, $I_{d,iso} F_{c-s}$ is the isotropic diffused contribution from the sky, $I_{d,cs} R_b$ is the circumsolar diffuse component coming from the same direction as the beam, and the fourth term $I_{d,hz} F_{hz-c}$ indicates the diffused contribution from the horizon band of area A_{hz}. In this paper, the point of interest is the fifth term $\sum_n I_n \rho_n A_n F_{n-c}$ that represents the reflected radiation from various sources such as trees, fields, buildings, and ground surfaces. However, to avoid complexity, we only consider the ground reflected radiation at the rear side of the module. Here I_n is the incident solar radiation on the ground surface n, and F_{c-n} is the view factor from PV collector c to ground n and ρ_n is the reflectivity or albedo of the surface n. Here, the term albedo is defined as (Iqbal, 1983),

$$Albedo, \rho = \frac{Reflected\ upward\ irradiance\ from\ the\ surface}{Incident\ downward\ irradiance\ on\ a\ surface}$$
$$= \frac{G_{REF}}{GHI} \tag{6}$$

If we consider only one ground surface, the reflected irradiance component of Eq. (5) becomes:

$$I_r = I \rho_{g1} F_{c-g1} \tag{7}$$

It is possible to enhance the reflected solar radiation incident on solar PV by using higher albedo surfaces such as white paint and sand surface (Gul et al., 2018). There can be multiple reflective surfaces present in an actual solar field, such as grass and soil. If we consider two reflective surfaces, then additional reflected irradiance from the second surface is $I \rho_{g2} F_{c-g2}$ where ρ_{g2} is the albedo of the second surface and F_{c-g2} is the view factor from solar PV to that surface. Then Eq. (5) becomes:

$$I_T = I_b R_b + I_{d,iso} F_{c-s} + I_{d,cs} R_b + I_{d,hz} F_{c-hz}$$
$$+ (I \rho_{g1} F_{c-g1} + I \rho_{g2} F_{c-g2}) \tag{8}$$

In this paper, a computation model is developed to calculate the view factor from a solar PV to any ground reflective surface. The following subsection discusses the view factor computation process for a uniform ground. It also explains the necessity of finite element methods for dealing with the non-uniform ground.

2.1. View factor computation for the uniform ground

Computation of the view factor for a uniform ground involves simple numerical integral, easily solvable by integration rules. The numerical integral for view factor was first obtained by (Hamilton and Morgan, 1952), who developed the expression for view factor computation (Eq. (9)). This expression was verified by Feingold, who provided the analytical solution of the view factor computation for the specific geometric condition (Feingold, 1966). The expression can be written as:

$$
\begin{aligned}
F_{1-2} = \frac{1}{\pi L} & \left[-\frac{1}{4} Sin2\varnothing \left[NLSin\varnothing + \left(\frac{1}{2}\pi - \varnothing \right) \left(N^2 + L^2 \right) \right. \right. \\
& \left. + L^2 tan^{-1} \left(\frac{N - LCos\varnothing}{LSin\varnothing} \right) + N^2 tan^{-1} \left(\frac{L - NCos\varnothing}{NSin\varnothing} \right) \right] \\
& + \frac{1}{4} Sin^2\varnothing ln \left\{ \left[\frac{\left(1 + N^2 \right)\left(1 + L^2 \right)}{1 + N^2 + L^2 - 2NLCos\varphi} \right]^{Cosec^2\varnothing + Cot^2\varnothing} \right. \\
& \left. \times \left[\frac{L^2(1 + N^2 + L^2 - 2NLCos\varnothing)}{\left(1 + L^2 \right)\left(N^2 + L^2 - 2NLCos\varnothing \right)} \right]^{L^2} \right\} \\
& + \frac{1}{4} N^2 Sin^2\varnothing ln \left[\left(\frac{N^2}{N^2 + L^2 - 2NLCos\varnothing} \right) \right. \\
& \left. \times \left(\frac{1 + N^2}{1 + N^2 + L^2 - 2NLCos\varnothing} \right)^{Cos2\varnothing} \right] + Ltan^{-1}\frac{1}{L} \\
& + Ntan^{-1} \left(\frac{1}{N} \right) - \sqrt{(N^2 + L^2 - 2NLCos\varnothing)} \\
& \times Cot^{-1}\sqrt{(N^2 + L^2 - 2NLCos\varnothing)} \\
& + \frac{N}{2} Sin\varnothing Sin2\varnothing \sqrt{\left(1 + N^2 Sin^2\varnothing \right)} \left[tan^{-1} \left(\frac{NCos\varnothing}{\sqrt{1 + N^2 Sin^2\varnothing}} \right) \right. \\
& \left. + tan^{-1} \left(\frac{L - NCos\varnothing}{\sqrt{1 + N^2 Sin^2\varnothing}} \right) \right] + Cos\varnothing \int_0^L \sqrt{\left(1 + z^2 Sin^2\varnothing \right)} \\
& \left[tan^{-1} \left(\frac{N - zCos\varnothing}{\sqrt{1 + z^2 sin^2\varnothing}} \right) \right. \\
& \left. \left. + tan^{-1} \left(\frac{zCos\varnothing}{\sqrt{\left(1 + z^2 Sin^2\varnothing \right)}} \right) \right] dz \right]
\end{aligned}
\tag{9}
$$

This numerical integral can be easily applied to compute the view factor for a uniform ground with minimum or no shadow present. In this paper, Eq. (9) has been applied to calculate view factor for uniform ground using three different numerical integration methods: midpoint rule, Simpson rule, and trapezoidal rule (Table 1). These three methods are chosen because these are widely used standard numerical integration techniques, which are computationally efficient and easy to code using software (Rammohan Rao and Sastri, 1996).

It will be improbable for real-life solar PV applications that the ground nearby will be completely uniform, and there is no shadow present around the field. Considering the practical utility of the computation tool, the need for developing a computation model that works in compliance with the non-uniform ground is essential. Hence, this work developed a finite element method based view factor computation model, which can handle the non-uniform ground of a bifacial solar PV field. Feingold's analytical solution is used for model verification throughout the paper (Feingold, 1966). The verification process is illustrated in Fig. 4. Here, the term extraction indicates the methodology used for computing the view factor, which is explained in Section 3.

3. Mesh generation algorithm

Mesh generation is an essential technique applied in various engineering applications. It represents any physical model in terms of partial differential equations (PDE). One of the widely used mesh generation methods is the finite element method (FEM) which is used for numerical simulation of the view factor computation in this paper (Okereke and Keates, 2018). The first step for such a simulation process requires building mesh around the physical computation domain, which replaces the continuous region into geometrically finite and straightforward elements of different shapes such as quadrilateral, triangle, tetrahedra, hexahedra. In this paper, a quadrilateral mesh is applied considering the rectangular geometry of the PV and ground surface.

To solve a mathematical model of view factor Eq. (2) with the FEM, we need to define the grid points to perform the discretisation. The grid can be uniform where the points are equally spaced point within the boundary. Another grid can be non-uniform or graded grid points in which the points can have different distributions along the axis dimension (Krysl, 2017). In this paper, we divided the total surface under consideration into two halves such that the lower half of the surface consist of fine mesh and the upper half consists of coarse mesh. We deployed a geometric progression (GP) series to generate the graded mesh throughout the surface under consideration where the geometric ratio is varied at slightly more than '1'. Hence, we name it quasi-uniform (almost uniform) grids. The advantage of this, it converges faster to the analytical solution than the uniform grid. Moreover, if we consider in the context of solar PV, the PV has a better view of the ground from its lower edge of the surface than the upper edge. The mesh generated can easily handle this as the grid points are clustered around the lower edge at a much higher density than the upper half of the surface. An efficient mesh generation must be computationally fast and accurate. Hence, the development of a numerical simulation model is a combined work of computational geometry of the generated mesh and the computing algorithm, which merges the field of computer science. One of the most fundamental paradigms in computer algorithms is the divide–conquer–combine technique (Cormen et al., 2001; Frey and George, 2010) which includes three simple steps of problem-solving such as:

- Consider a problem P and divide it into multiple segments, for example, P_1 and P_2.
- Solve the sub-problem P_1 and P_2.
- Merge the solution of two sub-problems.

This method was adopted innovatively for mesh generation for a PV system here and is described in the section below.

3.1. Divide–conquer–combine method for mesh generation

This section explains how the proposed geometric progression (GP) based mesh generation method applies the divide–conquer–combine algorithm to generate the fine and the coarse meshes. The steps are:

Step1 → Divide: Both the PV and the ground surface are divided into two rectangles. Here we assume the length and width of the PV surface are along the X and Y axis respectively. If the width of the surface is 1 m and length is 2 m, each half rectangle will be of width = 0.5 m and length = 2 m. For each half of the rectangle, the mesh is created by applying geometric progression (GP) as:

$$
a_n = a_1 r^{n-1}
\tag{13}
$$

where a_1 = the first term; a_n = the nth term, r = common ratio= $\frac{a_2}{a_1} = \frac{a_3}{a_2} = \frac{a_n}{a_{n-1}}$.

Table 1
Numerical integration method.

Integration rule	Mathematical presentation
Midpoint rule: In the midpoint method, a rectangle is constructed for each subinterval. The height of the rectangle lies at the midpoint of each sub-interval.	Mid-point integration formula for n sub-rectangles of equal width, h can be written as: $$\int_a^b f(x)\,dx = h\sum_0^{n-1} f(x_i); \text{ where } x_i = \left(a + \frac{h}{2}\right) + ih \qquad (10)$$
Simpson rule: Simpson's Rule is a numerical integration method for approximating definite signal. It is frequently used for integration in extended or compound form.	The expression of integration rule is written as: $$\int_{x_0}^{x_2} f(x)\,dx = \int_{x_0}^{x_{0+2h}} f(x)\,dx \approx \frac{1}{3}h(f_0 + 4f_1 + 4f_2) \qquad (11)$$ Here, function f(x) is calculated at two limits x_0 and x_{0+2h} at equally spaced distance h.
Trapezoidal rule: The trapezoidal rule estimates the definite integral in terms of the trapezoid instead of the rectangle to find the area under a curve.	If f(x) is continuous over the range [a,b] and [a,b] is divided into n sub-intervals with width h, then: $$\int_a^b f(x)\,dx \approx h\left[\frac{1}{2}f(x_0) + \sum_{i=1}^{n-1} f(x_i) + \frac{1}{2}f(x_n)\right] \qquad (12)$$
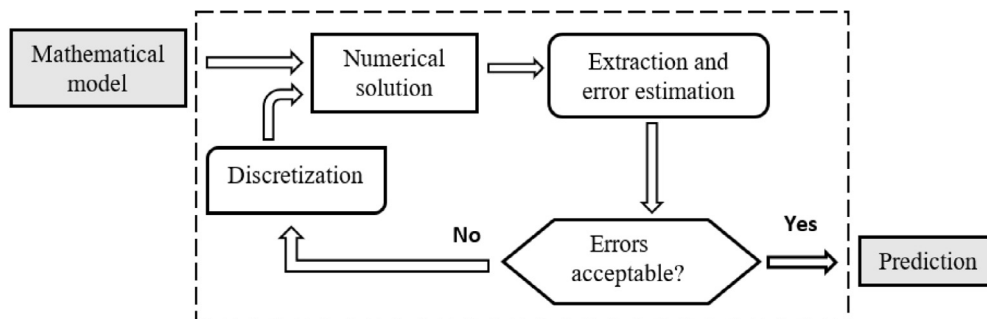
Fig. 4. Verification of the numerical solution (Szabó and Babuška, 2011).

Step2 → Conquer: The starting value of the geometric series to produce the upper half rectangular mesh is defined at first. This starting value is the element size for the first row of the upper half surface presented as $h_{0(Coarse)}$. The starting value of the coarse mesh is chosen such that the element size is some fraction of the surface length or width depending on whichever lies along the Y-axis, for example, in this case 0.4% of surface width. This % value is denoted by 'η'. The η% must be in the range that the view computation error remains below 1% level. For the lower half of the rectangle, the starting value of the element size is 50% of $h_{0(Coarse)}$ presented as $h_{0(fine)}$. By applying geometric progression, two sub-arrays are generated: $A[p_1 .. p_n]$ and $A[u_1 .. u_n]$, where u_1 is the halfway point of $A[p_1 .. u_n]$. With the total number of rows $= n$, the sum of geometric series can be written as:

$$S_n = a_1 \frac{(1 - r^n)}{1 - r}; r \neq 1 \qquad (14)$$

Here, S_n = sum of GP with n terms; a_1 = first term; r = common ratio of geometric progression; n = number of terms. For each subarray, the above summation is slightly less than the total width of the rectangle, $y/2$, which needs to be adjusted to maintain the accuracy of the calculation. Hence the last value of the series is determined using the formula:

last row width of rectangle

$$= \frac{y}{2} - \sum upper/lower \text{ geometric series} \qquad (15)$$

Now the total number of rows in the series becomes $n+2$ and each sub-array are now $A[p_1 .. p_{n+1}]$ and $A[u_1 .. u_{n+1}]$.

Step3 → Combine: The element size of the mesh has to increase gradually and cannot suddenly reduce at the end of the surface. Therefore, the mesh density must be maximum at the edge and gets lower at farthest from the edge. The geometric series is sorted in ascending order for both the upper and lower

half rectangle to match this. In this case, two sub-arrays $A[p_1 .. p_{n+1}]$ and $A[u_1 .. u_{n+1}]$ are sorted in an ascending order. By merging the two sorted sub-arrays, a single sorted sub-array $A[p_1 .. u_{n+1}]$ is produced. The flow chart of the mesh generation process is shown in Fig. 5.

3.2. Mesh analysis

The generated graded mesh is categorised as fine (lower half) and coarse (upper half). The transition between the finer mesh and coarse mesh region is called the grading factor. The boundary condition of each mesh is limited by the initial and final value of each rectangle. The element size (Fig. 6b) of the mesh is varied row-wise, unlike the uniform mesh in Fig. 6a, where the element size remains uniform throughout the surface.

To understand the quasi-uniform mesh concept, let us consider a mesh M_0 representing the first row of the lower half rectangle. The element size of the grid for the first row is denoted by $h_0(x)$. Then produce a GP series by scaling the element size as a function of surface width 'y' at a common ratio r_1 where r_1 is slightly greater than 1 everywhere in the domain. The element size of mesh M_1 (the second row) can therefore be defined as $r_1 \cdot h_0(x)$ and for M_2 as $r_1 \cdot h_1(x)$. We can, therefore, write:

$$\lim_{x=0 \text{ to } l} h_{i+1}(x) = r_1^i \cdot h_0(x); i = 0 \text{ to } N \qquad (16)$$

$$\lim_{x=0 \text{ to } l} h_1(x) = r_1 \cdot h_0(x) \qquad (17)$$

$$\lim_{x=0 \text{ to } l} h_2(x) = r_1 \cdot h_1(x) = r_1^2 \cdot h_0(x) \qquad (18)$$

The common ratio is held constant for each half of the rectangle (fine mesh and coarse mesh section). If the common ratio of coarse mesh is assumed as r_2, then the grading factor between the fine and coarse mesh is calculated as,

$$Grading\ Factor, GF = \frac{r_2}{r_1} \qquad (19)$$
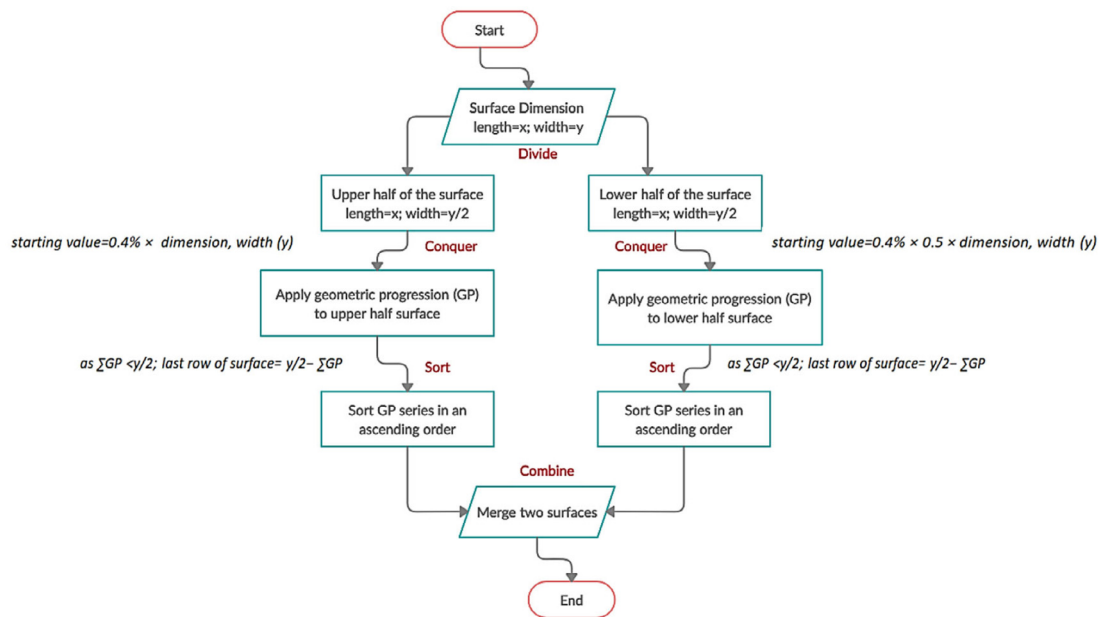
Fig. 5. Mesh generation process based on 'divide–conquer–combine' algorithm.

Length of the grid, X

Width of the grid,

Fig. 6a. Uniform grid with grading factor = 1.

Length of the grid, X

Width of the grid, Y
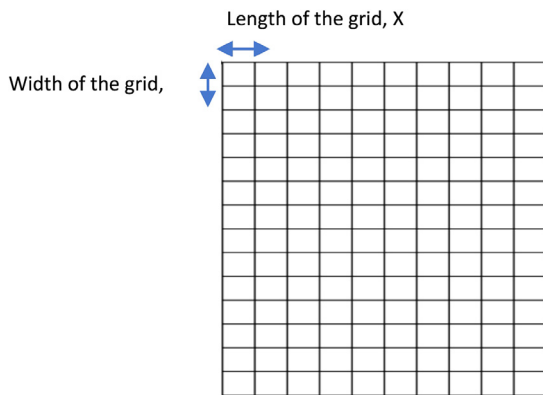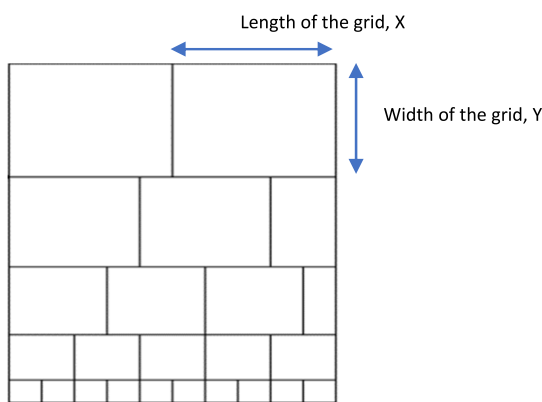
Fig. 6b. Non-uniform grid with grading factor > 1.
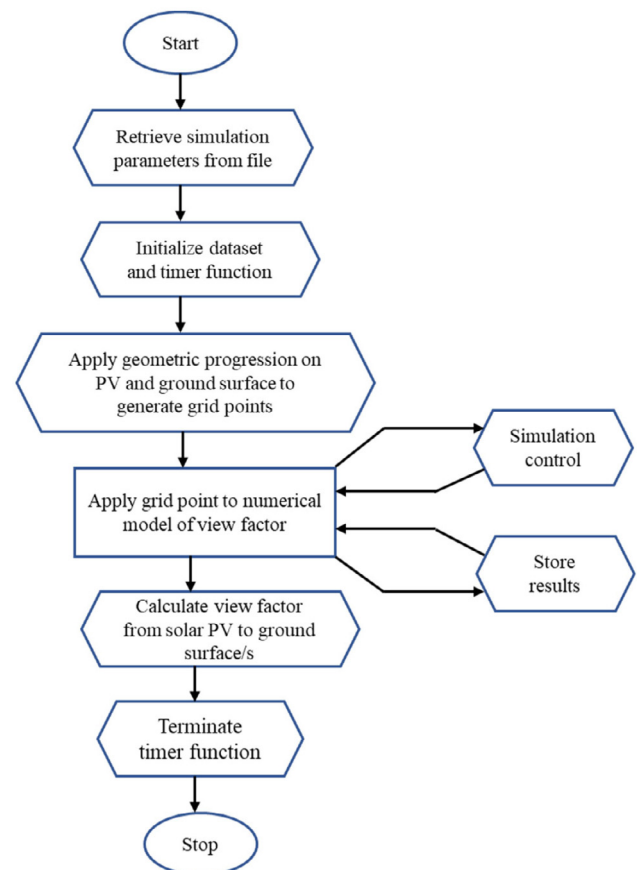
Fig. 7. Flow chart of the simulation model.

The common ratio r_1 and r_2 is varied at slightly more than '1' to keep the element size of the grid almost uniform but to vary along the surface. The gradual changes of grid size prevent loss of accuracy due to gradation itself. The mesh generated in this way is applied to the view factor simulation model. The computation error of the view factor depends on two factors: i. the smallest element size (the first value of the geometric series) of the geometric series of the coarse mesh (upper half surface) determined by $\eta\%$ and, ii. The grading factor between fine and coarse mesh. These are further discussed in Section 4.
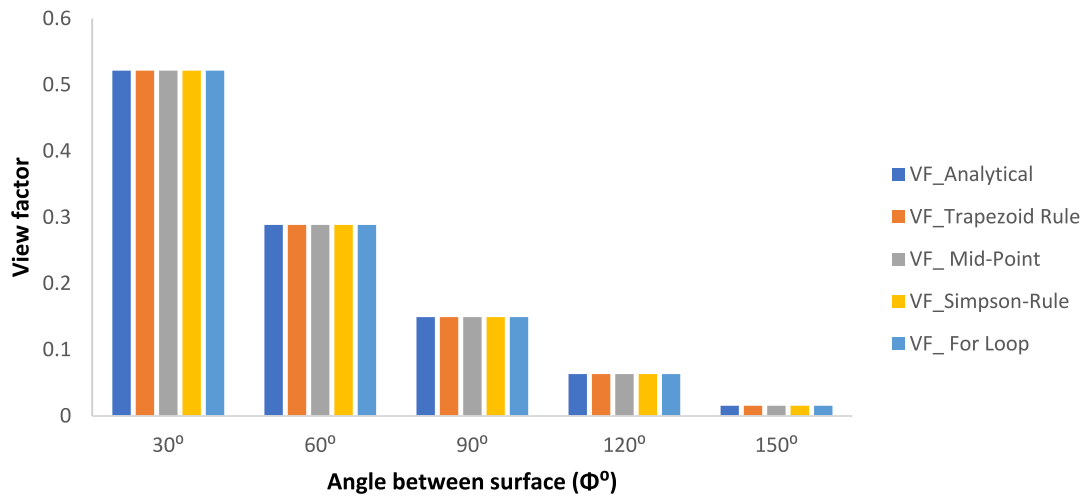
Fig. 8. View factor computation for uniform ground using integration rule.
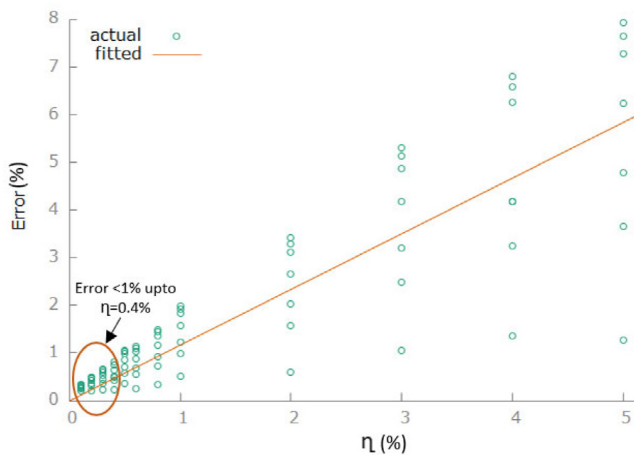
Fig. 9. Actual Vs fitted error at a different grid size.

3.3. Overview of the simulation framework

The view factor simulation model is developed in Python version 3.7 at Spyder integrated development environment (IDE). The model utilises numerically intensive computing Python library, 'Numba', which can be loaded by the program as a Cpython interpreter. It is an open-source just-in-time (JIT) compiler which converts the Python and NumPy subset into faster machine code via the low-level virtual machine (LLVM) Python package. The compiler creates a specialised loop in machine code. The just-in-time is a decorator, which works like a function. During the function call, the decorator interprets the argument and generates a specialised function (Lam et al., 2015). The code is then executed on 'nopython' mode, which compiles the code without accessing the Python C-API (application program interface). The simulations are run on Intel® Core™ i7-7500U CPU @ 2.9 GHz Laptop. The simulation flow chart is shown in Fig. 7.

4. Results and analysis

In this paper, the developed view factor computation model is tested for nine different cases displayed in Table 2. Case 1 represents the simple solution of view factor computation for uniform ground via numerical integration rule (Table 1). Following

that, case 2 focuses on verifying the numerical model for non-uniform ground by testing the hypothesis, determining coarse to fine mesh ratio, convergence test and regression analysis. Case 3 analyse the computation error and computation time dependency of the model. Cases 4–10 consider view factor variation at different PV field scenarios. Here, two assumptions are applied throughout the calculation.

- All the calculation assumes bifacial PV and its view factor to the ground at the rear side of the PV module. However, similar results are replicable for the view factor to the ground at the front side of both the bifacial and monofacial PV module.
- The unit of x, y, and z-axis shown in Figs. 2, 3, 14, 17, 19, 21, 23 and 26 is assumed in metre (m).

4.1. Case 1: Integration rule for a uniform ground

In this section, three different integration methods, trapezoidal rule, Simpson method, and mid-point rule, as explained in Table 1, have been applied to compute the view factor for a uniform ground. Numerical integration is run for different tilt angles of solar PV, which vary between 30°–150°. From Fig. 8, it can be seen that in all cases, the results are computationally highly accurate compared to the analytical output, and the accuracy is close to 100%. The computation time is also faster, which is as low as 10 ms.

4.2. Case 2: View factor model verification for the non-uniform ground

4.2.1. The hypothesis to determine the element size of the grid

For the selection of the element size of the grid in the finite element mesh, a hypothesis is set as: The smallest element size (the first value of the geometric series) of the coarse mesh (upper half rectangle) should not be more than $\eta = 0.1\%$–0.4% of the surface width where the width of the surface is along the Y-axis. If the length of the surface is along the Y-axis, then, $\eta = 0.1\%$–0.4% of the surface length. The view factor computation error increases beyond 1% above the $\eta = $ value of 0.1% to 0.4%.

To test the hypothesis, a regression analysis is run between the computation error versus the 'η' value (Fig. 9). It appears that the circled region in the graph is within the range of η value = 0.1% to 0.4%. Up to this range, the view factor computation error is below 1%. Beyond this, the error rises considerably.
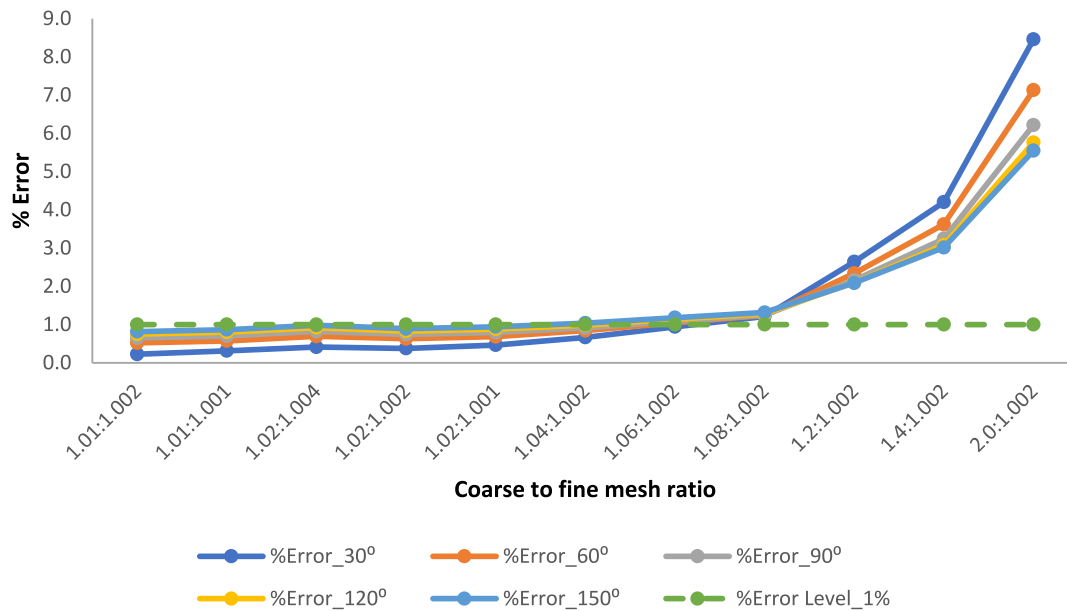
Fig. 10. %Error at different tilt angles for various fine to coarse mesh ratio.

Table 2
Cases considered in the present work.

Case no.	
Case 1	Integration rule for a uniform ground
Case 2	Model verification for non-uniform ground:
	• Testing hypothesis for element size determination for a quasi-uniform mesh
	• Determination of coarse to fine mesh ratio (grading factor)
	• Convergence test
	• Regression analysis (R^2 test)
Case 3	Error versus time optimisation
Case 4	View factor to non-uniform ground surfaces
Case 5	View factor variation along the PV surface
Case 6	View factor variation with the ground clearance height (GCH) of solar PV
Case 7	View factor to the inclined ground surface
Case 8	View factor at different position of PV with respect to the ground reference
Case 9	Sensitivity of view factor with ground length and width
Case 10	View factor at different PV string length

Table 3
Regression to determine the significance of 'η' value.

OLS regression results			
Dep. variable	Error (%)	*R*-squared (uncentred):	0.886
Model:	OLS	Adj. *R*-squared (uncentred):	0.882
Method:	Least Squares	F-statistic:	210.2
Date:	Wed, 21 Ap2021	Prob (F-statistic):	2.92e−14
Time:	01:15:59	Log-likelihood:	12.302
No. observations:	28	AIC	−22.60
Df residuals:	27	BIC:	−21.27
Df model:	1		
Covariance type:	nonrobust		

	coef.	std err	*t*	*P* > |*t*|	[0.025	0.975]
η (%)	1.589	0.11	14.5	0.000	1.364	1.814

Furthermore, another ordinary least square regression (OLS) test (Sarmento and Costa, 2017) is conducted in Python with the 'η' value of 0.1%–0.4% to determine the *p*-value to prove the significance of the above hypothesis. The results obtained from the ordinary least square regression can be found in Table 3 below. It is found that the *p*-value (0 < 0.001) is statistically highly significant, which confirms that the above hypothesis regarding element size for mesh generation is correct. Moreover, the R^2 value is close to 0.9, indicating that 90% of the computation error (dependent variable) can be explained by the independent variable 'η'.

4.2.2. Determination of coarse to fine mesh ratio (grading factor)

Section 4.2.1 has established the acceptable ranges of η% to retain the error level below 1%. In this section, we examined the computation error at different common ratios of geometric progression to identify the grading factor (*GF*) between the coarse and fine mesh. Here, the 'η' value is held within the acceptable range of 0.1%–0.4%. The common ratio of fine and coarse mesh is varied in the range of 1.001–1.002 and 1.01–2, respectively, to identify the acceptable grading factor ranges (Table 4) for the computation model.

The computation error at a different angle for various coarse to fine mesh ratios is presented in Fig. 10. Here, the angle between

Table 4
Grading factor at different fine to coarse mesh ratio.

Ratio_fine mesh, r_1 for lower half surface	Ratio_coarse mesh, r_2 for upper half surface	Grading factor, $= \frac{r_2}{r_1}$
1.002	1.01	1.008
1.001	1.01	1.009
1.004	1.02	1.016
1.002	1.02	1.018
1.001	1.02	1.019
1.002	1.04	1.038
1.002	1.06	1.058
1.002	1.08	1.078
1.002	1.2	1.198
1.002	1.4	1.397
1.002	2	1.996

Table 5
Comparison of view factor computation outputs at different iteration size.

Grading factor (r_2:r_1)	View factor	%Error	Elements	Iterations	Computation time (s)
2:1.3	0.45926786	11.9%	1.33E+03	1.77E+06	1.14
1.2:1.003	0.507450108	2.66%	3.67E+04	1.35E+09	36.42
1.02:1.002	0.519344984	0.314%	4.66E+04	2.17E+09	83.33
1.01:1.002	0.520127435	0.226%	4.90E+04	2.40E+09	98.69
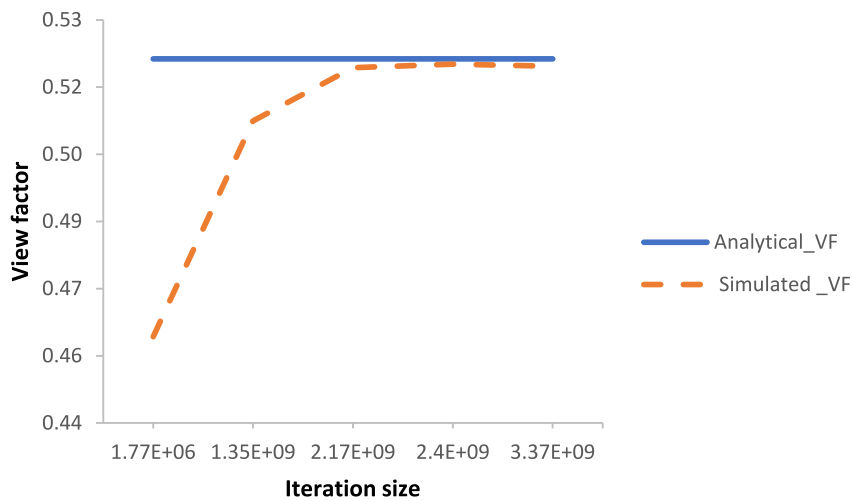
Fig. 11. Convergence of view factor to the analytical solution.
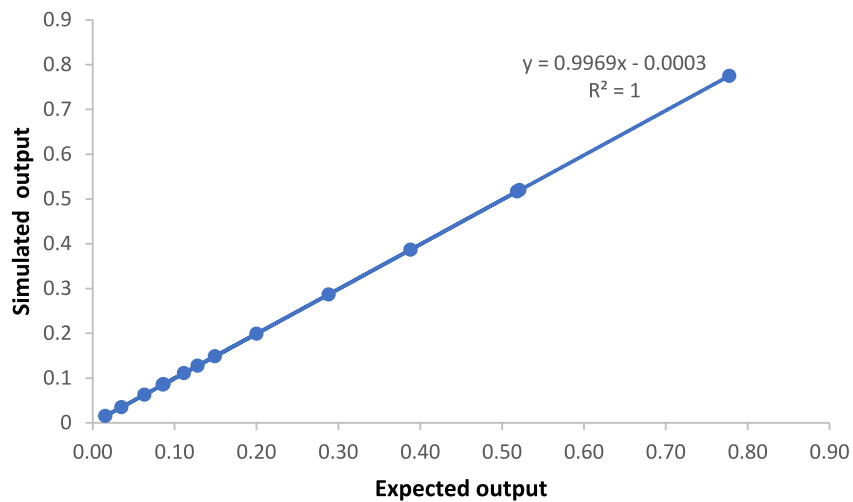
Fig. 12. Regression analysis between expected and simulated output.

Table 6
View factor from PV to multiple reflective surfaces.

Coordinate of grass surface	VF from PV to the soil surface	VF from PV to the grass surface	Computation time (s)
[(1,1,0), (4,1,0), (5,2,0), (2,2,0)]	3.41E−02	5.44E−01	239.30
[(1,1,0), (5,1,0), (5.8,3,0), (2,3,0)]	8.84E−02	4.90E−01	220.93
[(1,1,0), (2,1.2,0), (2,3.5,0), (1,3.8,0)]	1.26E−01	4.53E−01	182.78
[(1,1,0), (5,2,0), (5.5,3,0), (2,3,0)]	4.88E−02	5.3E−01	241.05
[(1,1,0), (5.8,0), (5.9,3.8,0), (0,3.8,0)]	5.56E−01	2.3E−02	201.97

Table 7
Computation time and iteration size for view factor calculation at different PV string length.

PV width	String length	Ground width	Ground length	View factor	Iteration size	Computation time (s)
2	20	5	40	8.65E−01	7.65+11	15409
2	15	5	30	8.64E−01	4.30E+11	9391
2	10	5	20	8.63E−01	1.91E+11	3995
2	5	5	10	8.57E−01	4.78E+10	1107
2	4	5	8	8.51E−01	3.06E+10	689
2	2	5	4	7.28E−01	7.67E+09	180
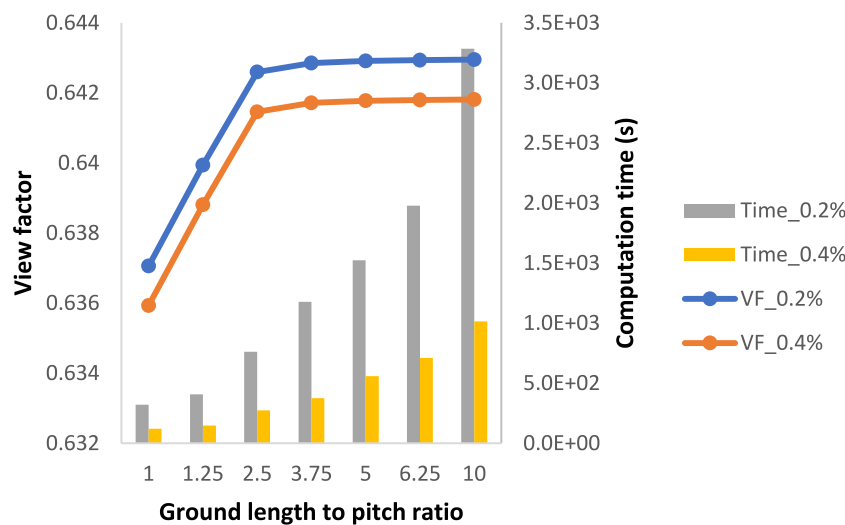
Fig. 13. View factor variation at different ground length to pitch ratio.

the PV and ground surface is varied from 30°–150°. The most accurate result is obtained at a grading factor of $GF = 1.008$, where the % error is minimum at 0.226%. This finding is reasonable because, at this grading factor, the value of the fine and coarse grid is $r_1 = 1.002$ and $r_2 = 1.01$ respectively, which makes it an almost uniform or quasi-uniform grid. For all the angles considered here, up to the grading factor of 1.038, the % error remains below 1%, but it starts to increase beyond that, and at $GF = 2$, the computation error goes beyond 8%. Therefore, the acceptable ranges of fine and coarse mesh ratio should be in the range of (1.001–1.002) and (1.01–1.04), respectively.

4.2.3. Convergence test

The most extensive test of a code and algorithm's accuracy for a simulation-based code is the convergence test. It determines the rate at which the code approaches an analytical solution which can be computed as:

$$\beta = \exp(\frac{log\left(e_{rrk_1}/err_{k_2}\right)}{k_1/k_2}) \qquad (20)$$

Here, β represents the rate of convergence, k_1 and k_2 are the iteration sizes of view factor computation where $k_1 > k_2$ and err_{k_1}, err_{k_2}, are the error at iteration size k_1 and k_2, respectively. The convergence of view factor simulation to the analytical solution is studied at different grading factors between upper and
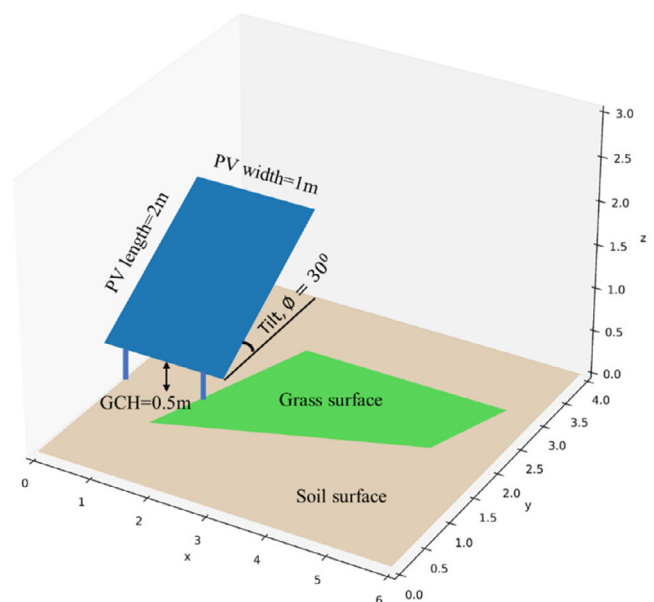
Fig. 14. The non-uniform ground surface consists of soil and grass.
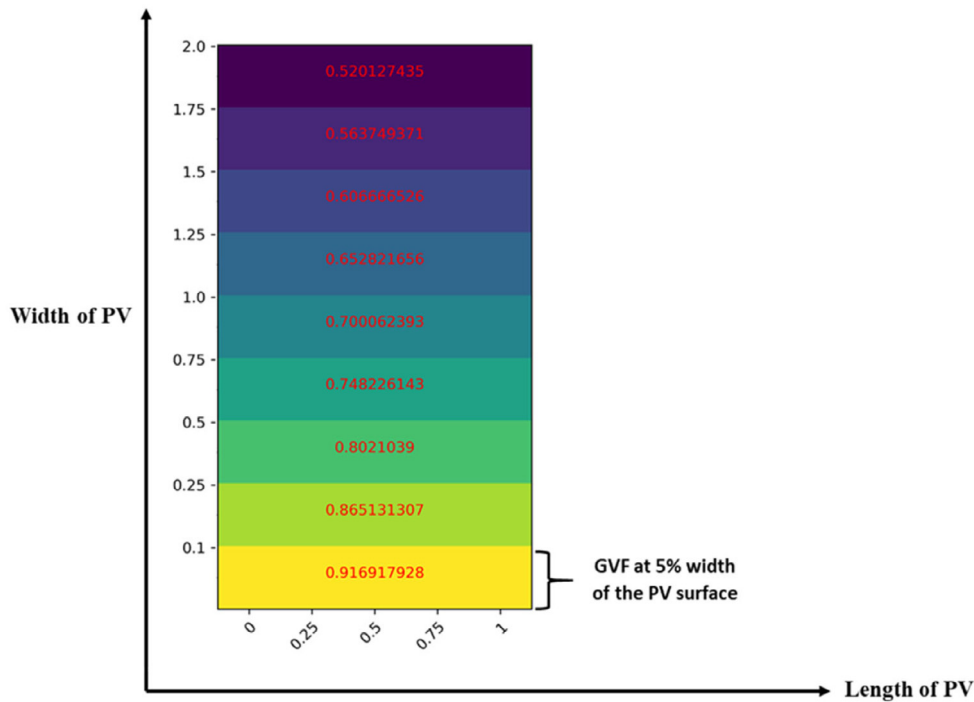
Fig. 15. Variation of view factor along the surface of solar PV.
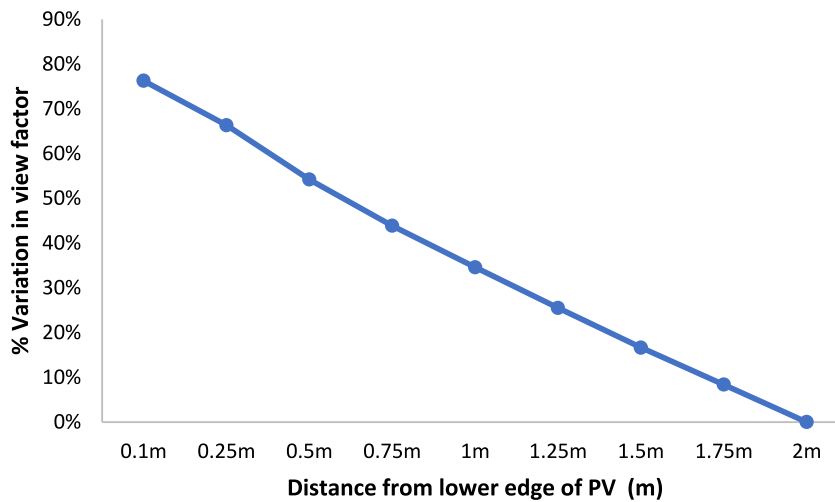
Fig. 16. %Variation in view factor with the distance from the lower edge of PV.

lower half meshes of the surface. Based on the value of the grading factor, the iteration size of the computation varies. In Fig. 11, we can see that view factor computation accuracy improves at a faster rate as the iteration size increases from 1.77 million to 1.35 billion. As the iteration size rises from 1.35 billion to 2.17 billion, the view factor output converse towards the analytical solution at a rate of 0.59. However, the VF output has a slight change as the iteration size further increases towards 2.4 billion.

Table 5 shows a comparison among view factor output, computation error, computation time and the total number of elements at different iteration sizes. It is important to note that any numerical solution demands two things: accuracy and computation time or the CPU response time. There is a substantial reduction in the error from 11.9% to 0.226% as the iteration size increases from 1.77 million to 2.4 billion (11.9%). However, the computation time increased by 87 times more to reduce the error to 0.226%.

4.2.4. Regression analysis between simulated vs expected view factor output

Based on the finding in Sections 4.2.1–4.2.3, a regression analysis is performed between the expected output obtained from the analytical solution and the simulated output of the view factor. Fig. 12 shows a perfect fit that the analytical and simulated response completely fits each other with an R^2 value equal to 1.

4.3. Case 3: Error versus time optimisation

One of the challenges of the view factor computation model is, with increasing ground length, the computation time also increases considerably. Hence it requires optimising the code such that the accuracy of the computation is retained at a reasonable level, and the computation time is also faster. In Fig. 13 below, the row-to-row distance between solar PV (also known as the pitch) is = 4 m, the ground length is varied from 4 m to 40 m. The
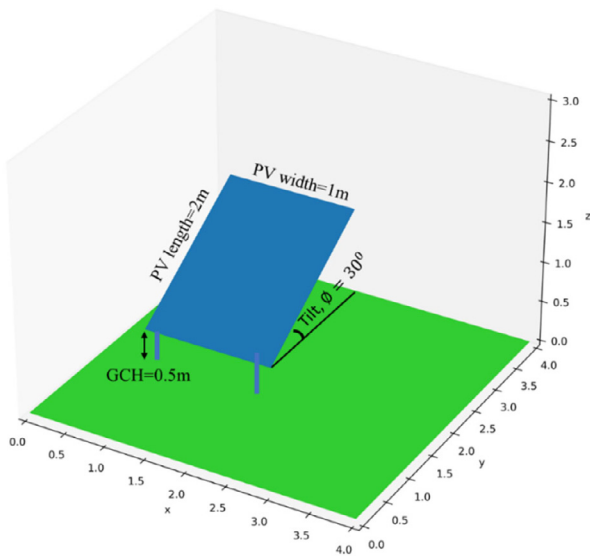
Fig. 17. Solar PV at a ground clearance height (GCH) of 0.5 m.

tilt angle of PV is $\Phi = 30°$, PV length $= 2$ m along the Y-axis and width $= 1$ m along the X-axis and the PV height $= 0.25$ m. In the mesh generation process, we considered the minimum element size of the grid for the PV=0.004. For the ground surface, the result is repeated with the element size, $h = 0.004$ ($\eta = 0.2\%$) and $h = 0.008$ ($\eta = 0.4\%$). For both cases, the view factor changes linearly up to a certain ground length to pitch ratio of 2.5 in this case, and after this ratio, the view factor almost remains constant with the increasing ground length up to 40 m. However, the computation time at η=0.2% is three times more ($t = 3284$ s) than the computation time at $\eta = 0.4\%$($t = 1014$ s). Therefore, considering the time constraint, $\eta = 0.4\%$ will be a reasonable choice for this case.

4.4. Case 4: View factor to non-uniform ground surfaces

A non-uniform ground indicates where the surface changes in an irregular pattern. For example, a ground comprising more than one surface of different albedos, such as a combination of plain grass and soil, is shown in Fig. 14. The integration method explained in 4.1 is not applicable here, as the view factor need to be computed separately for the grass and soil surface. Therefore, it applies the view factor computation model and calculates the view factor from solar PV to the grass surface and the view factor from solar PV to soil surface separately.

In this case, the view factor is computed for different coordinates of the grass surface, as shown in Table 6. Here the tilt of the PV panel is considered, $\Phi = 30°$. The PV is positioned at a co-ordinate of ($x = 0$, $y = 0$, $z = 0.5$) and the co-ordinate of soil surface is kept at[(0,0,0),(6,0,0),(6,4,0),(0,4,0)].

4.5. Case 5: View factor variation along the PV surface

This section presents the view factor variation along the PV surface width (along the Y-axis), illustrated in Fig. 15. It is found that the view factor is the highest (about 0.92) for up to 5% of the surface width. The view factor decreases if it is seen farthest from the lower edge of the PV surface. Thus, for the total surface width, the VF is about 0.52. The variation of colours in this surface plot signifies the intensity of the view factor, which means, lighter the shades (yellow), the higher the view factor.

Moreover, this variation is 76% more from the lower cells for a PV width of 2 m (Fig. 16). This finding implies that solar PV cells closer to the ground will have a better view of the ground surface than the cells at the upper edge along the width of the PV.

4.6. Case 6: View factor changes with the ground clearance height (GCH) of solar PV

The height of the PV module has an impact on the view factor. The view factor from solar PV to ground (GVF) indicates an inverse dependency on the ground clearance height (GCH). Here, GCH represents the vertical height from the ground to the lower edge of the PV panel. In this case, the GCH is varied from 0.1 m to 1.25 m. A solar PV at GCH $= 0.5$ m and tilt $= 30°$ is shown in Fig. 17.

We can see from Fig. 18 that the view factor from solar PV to ground (GVF) is at its maximum when the GCH $= 0.1$ m, which is 4.47E−01. However, as the height increases, the ground view factor decreases by 21.78% (GCH $= 0.25$ m) to 94.6% (GCH $= 1.25$ m). This implies,

$$GVF \propto \frac{1}{GCH} \tag{21}$$

4.7. Case 7: View factor to the inclined ground surface

In all the previous sections, the view factor was calculated for the flat ground surface at a slope of 0°. In this section, a 10° upward and 10° downward slope of the ground surfaces are considered. Fig. 19 presents 10° upward sloped ground that is inclined towards the PV. The tilt angle of the solar PV with respect to the flat ground is varied from 20° to 90°. Therefore, if the angle between solar PV and the flat ground surface is 30°, the angle between that solar PV and the 10° upward tilted ground surface will reduce to $(30° - 10°) = 20°$.

Due to the decrease in angle between solar PV and ground, the view factor from solar PV to ground increases by 11% to 47% compared to the view factor at the flat ground (Fig. 20). However, if we consider 10° downward sloped ground where the ground is inclined in the opposite direction of solar PV, the view factor decreases with respect to flat ground by about 11%–22% due to an increase in the angle between solar PV and ground.

4.8. Case 8: View factor at a different position of PV with respect to the ground reference

Depending on the solar PV position with respect to the reference ground, the view factor shows a changing pattern. In this case, the solar PV position is varied from the starting edge of the reference ground, $x = 0$ m up to the total length of the ground, $x = 10$ m. A solar PV placed at a 5 m distance from the ground reference is shown in Fig. 21. The available area to PV for all the cases is 40 m^2.

If the PV is placed at $x = 1$ m distance from the ground edge, then the view factor increases by 23.88%. However, after the distance of $x = 1$ m, the rear-view factor changes at a slower rate, and the maximum value is reached at $x = 5$ m. Beyond the distance of $x = 7$ m, the view factor continues to decrease (Fig. 22). The view factor is maximum (8.3E−01) at half point between the ground length, in this case at $x = 5$ m. This is understandable as, at a 5 m distance from ground reference, a solar PV sees an equal portion of the ground area on both sides.
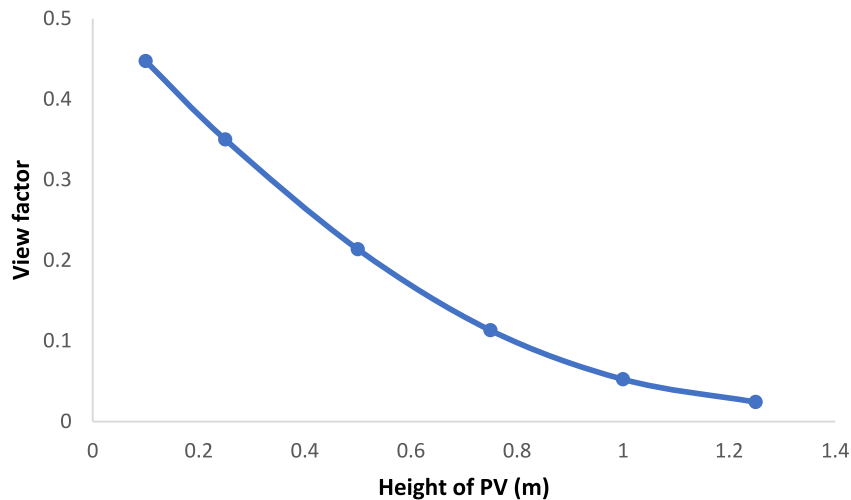
Fig. 18. View factor at different heights of PV.
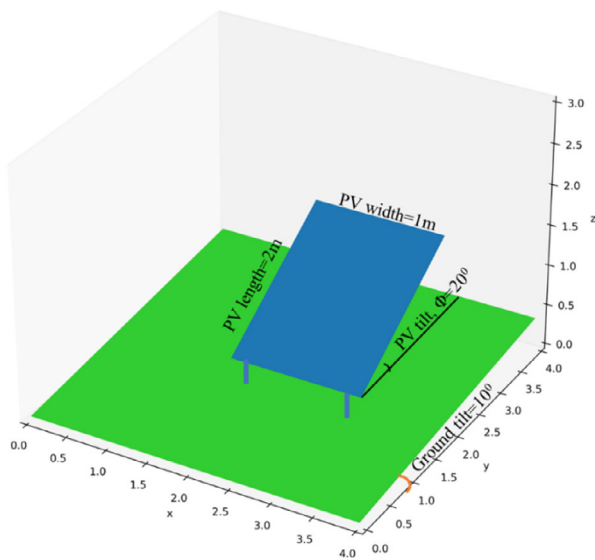
Fig. 19. Solar PV on 10° tilted upward ground surface.

4.9. Case 9: Sensitivity of view factor with the ground length and width

In this section, we varied the ground length and width separately for the fixed PV string length and width to analyse the sensitivity of the view factor with respect to the dimension of ground. Here a PV string of 5 modules is considered. First, the ground width is kept fixed at 5 m, and the length is varied along the *x*-axis from 6 m to 25 m. Then the ground length is held unchanged at 8 m, and the ground width is changed along the *y* axis from 4 m to 22 m. A single PV string with an available rear ground area of 80 m² is shown in Fig. 23.

It can be seen in Figs. 24 and 25 that, up to 8 m distance from the PV position, the view factor tends to increase by about 7%. Within 8 m to 10 m distance, the view factor rises at a slower rate. However, the benefit for extended ground coverage diminishes beyond 10 m distance from solar PV position, and the changes in view factor remain almost steady. Therefore, a reasonable length and width of 8 m would be optimum, up to which the view factor can be considered significant. This finding is essential for bifacial PV system design to calculate the amount of ground coverage required if enhanced irradiance gain using a reflective ground surface with higher albedo is expected.

4.10. Case 10: View factor of PV string of variable length

This section considered PV string of variable length to understand the changes of view factor with the string length size. The string length is varied from 2 m to a maximum of 20 m, and the distance between the two consecutive strings is kept as 5 m. The ground area is considered five times the area of the PV string. Two PV strings of 5 m length are displayed in Fig. 26, where string1 has an available rear ground area of 70 m². It is essential to define the maximum PV string length, which is practically feasible to evaluate a large PV string's view factor. Usually a single PV string of a maximum 1000 V is technically feasible for an actual PV field (Gkoutioudi et al., 2013). Therefore, the open circuit voltage of each PV is assumed 43.5 V to keep the string voltage below 1000 V.

The computation requirement at various string lengths of solar PV and the corresponding view factor values are presented in Table 7.

5. Conclusion

The reflected irradiance at bifacial solar PV depends on the view factor from PV to ground. For the rear side of bifacial PV, accurate computation of view factor is critical due to the non-uniformity of irradiance at the rear side of the PV. The existing analytical methods of view factors calculations are often limited to certain geometries and may not handles non-uniform geometries efficiently. Moreover, the analytical method is computationally intensive which is not solvable manually for higher-order numerical values. Hence, we have proposed this computation model, which uses the analytical solution as a benchmark to verify our model. This model applies geometric progression based finite element mesh in the mathematical model of view factor. By considering different orientations of the PV modules at the solar PV field, the view factor is estimated by dividing both the PV and ground surface into meshes/grids. Then statistical regression method is applied to determine the accuracy of the estimates. The view factor model is analysed under six geometric variables: multiple reflective ground surfaces, the height of PV, tilted ground surface, PV position in the ground, length and width of the ground, and PV string length. However, to avoid added complexity, the shape of the nearby structure or any object which can obstruct the ground view has been ignored. The key findings of this work are:
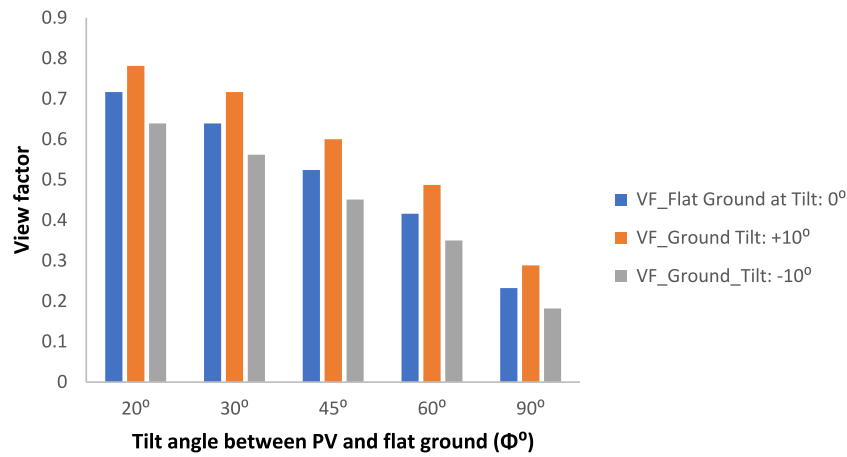
Fig. 20. View factor variation of the tilted ground surface.
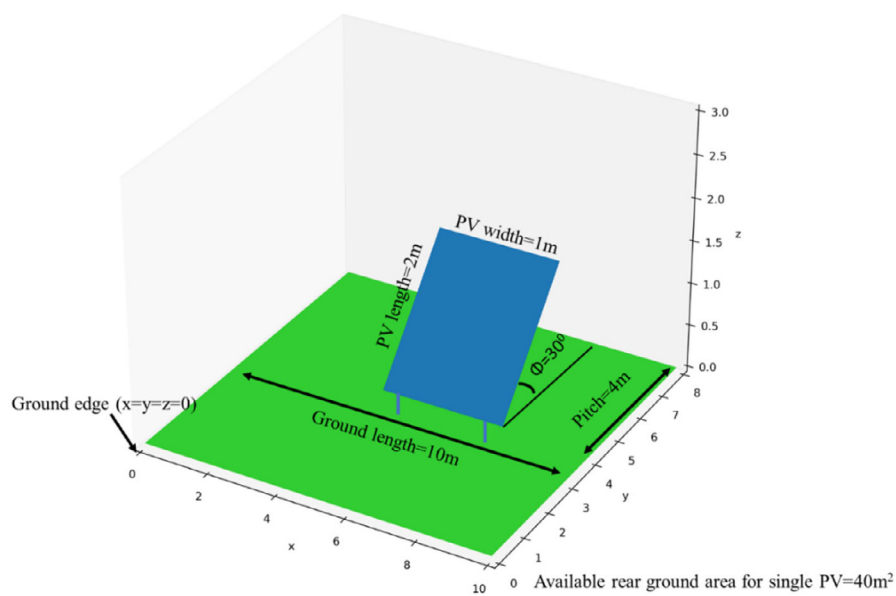
Fig. 21. Solar PV at 5 m distance from the ground reference.
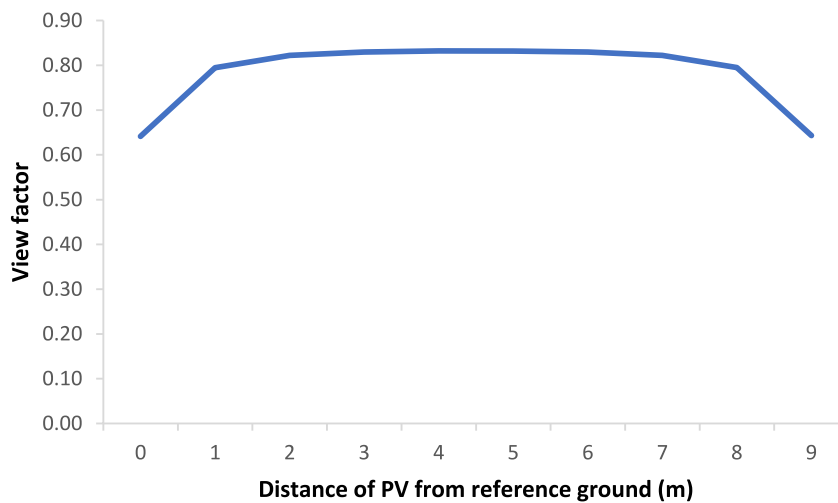
Fig. 22. View factor variation due to distance of PV from the reference ground.
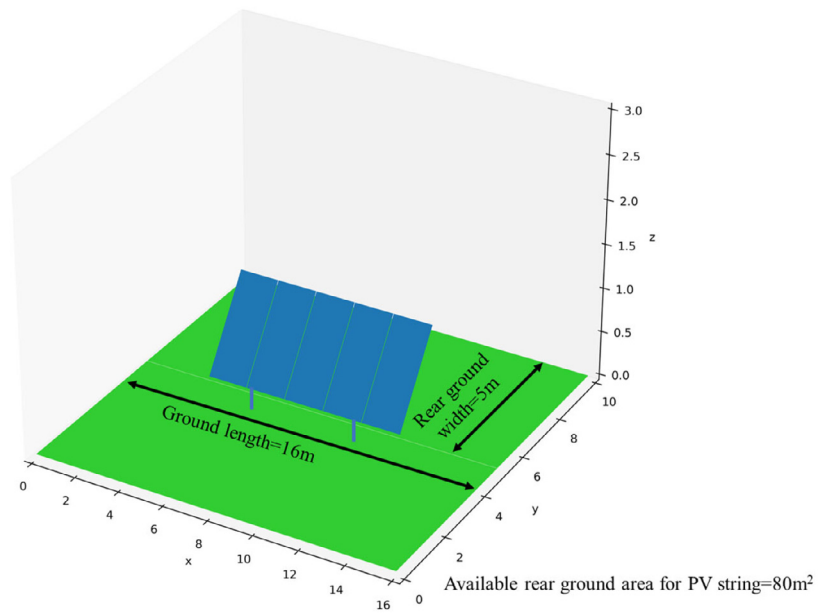
Fig. 23. Single solar PV string with the available rear ground area of 80 m².
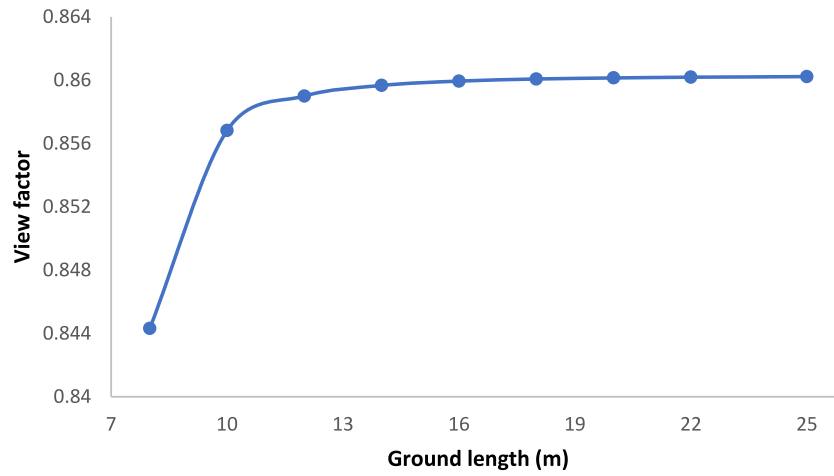
Fig. 24. View factor variation at different ground length.
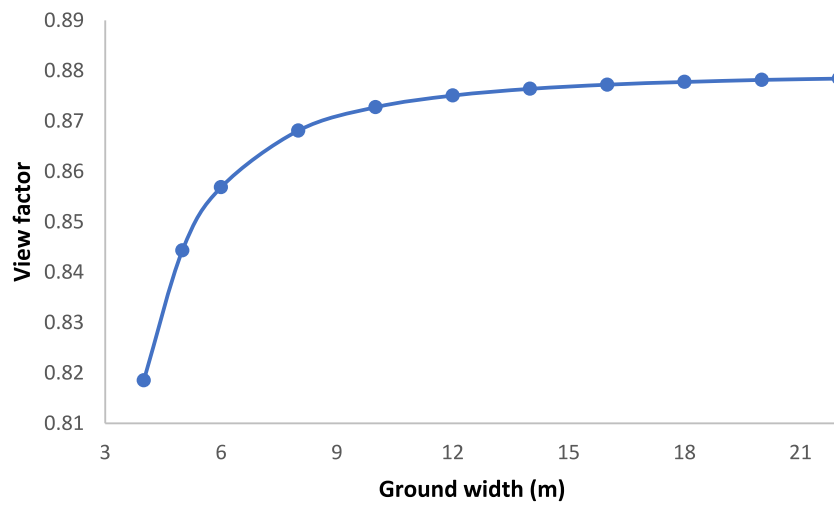
Fig. 25. View factor variation at different ground width.
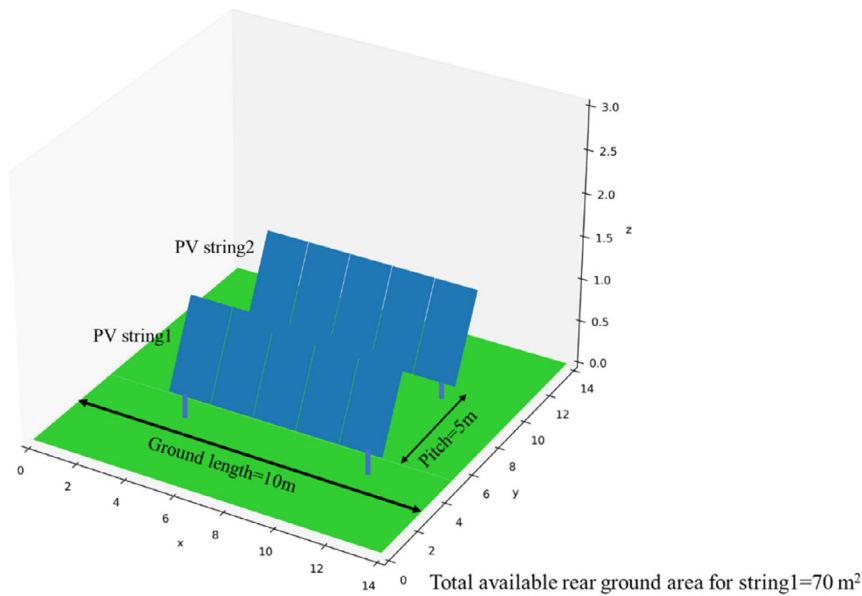
Fig. 26. Multiple solar PV string with the available rear ground area of 70 m².

- The view factor computation model provides an accuracy level of 99%.
- To retain accuracy at the 99% level, the smallest value of the element size of the coarse mesh should be in the range of 0.1%–0.4% of the surface length or width (whichever lies along the Y-axis), and the ranges of grading factor of the fine and coarse mesh are 1.001–1.002 and 1.01–1.02 respectively.
- The view factor to the ground at the rear side of bifacial PV shows an inverse relationship with the increased ground clearance height of solar PV.
- Solar PV cells closer to the ground will have a better view of the ground surface than the cells at the upper edge along the width of the PV.
- The rear side view factor of bifacial PV to the upward tilted ground surface is 11%–47% more than its view factor to a flat ground surface but 11%–22% lower for downward tilted ground due to an increase in the angle between solar PV and ground.
- The rear side view factor of bifacial PV is maximum if the PV is placed halfway between the total available ground length.
- It is found that, up to 8 m distance from the PV position, the view factor tends to increase and beyond the 10 m distance view factor remains almost unchanged.
- For string level analysis, the ground area varied from 20 m²-200 m². For these respective areas, the view factor computation time varies in the range of 180 s with an iteration size of 7.67 billion to 15409 s (257 min) for the iteration size of 765 billion.

To conclude, the outcome of this work can have an essential contribution to the solar PV research community for designing bifacial systems and analysing the irradiance gain of bifacial PV. For the developer and investor, the finding of this paper is beneficial to determine the amount of ground coverage required in a solar field if the ground surface albedo need to be augmented by using highly reflective surfaces.

Declaration of competing interest

The authors declare that they have no known competing financial interests or personal relationships that could have appeared to influence the work reported in this paper.

References

Alam, M., Gul, M.S., Muneer, T., 2019. Radiation view factor for building applications: Comparison of computation environments. Energies.

Alam, M., Gul, M.S., Muneer, T., 2021. Self-shadow analysis of bifacial solar photovoltaic and its implication on view factor computation. In: IEEE Green Energy and Smart Systems Conference (IGESSC). pp. 1–5. http://dx.doi.org/10.1109/IGESSC53124.2021.9618684.

Appelbaum, J., 2016. View factors to grounds of photovoltaic collectors. J. Sol. Energy Eng..

Appelbaum, J., 2018. The role of view factors in solar photovoltaic fields. Renew. Sustain. Energy Rev..

Appelbaum, J., Aronescu, A., 2016. View factors of photovoltaic collectors on roof tops. J. Renew. Sustain. Energy.

Arthur, D.W., Davis, P.J., Rabinowitz, P., 1986. Methods of numerical integration. Math. Gaz..

Asgharzadeh, A., et al., 2019. A benchmark and validation of bifacial PV irradiance models. In: Conference Record of the IEEE Photovoltaic Specialists Conference.

Cormen, T.H., Leiserson, C.E., Rivest, R.L., 2001. Introduction To Algorithms, second ed..

Dirksen, M., Ronda, R.J., Theeuwes, N.E., Pagani, G.A., 2019. Sky view factor calculations and its application in urban heat island studies. Urban Clim..

Duffie, J.A., Beckman, W.A., 2013. Solar Engineering of Thermal Processes, fourth ed..

Fathi, N.Y., Samer, A., 2016. View factors of flat solar collectors array in flat, inclined, and step-like solar fields. J. Sol. Energy Eng. Trans. ASME.

Feingold, A., 1966. Radiant-interchange configuration factors between various selected plane surfaces. Proc. R. Soc. London A Math. Phys. Eng. Sci. 292 (1428), 51–60.

Francisco, S.C., Raimundo, A.M., Gaspar, A.R., Oliveira, A.V.M., Quintela, D.A., 2014. Calculation of view factors for complex geometries using Stokes' theorem. J. Build. Perform. Simul..

Frey, P.J., George, P.L., 2010. Mesh Generation: Application To Finite Elements, second ed..

Gkoutioudi, E., Bakas, P., Marinopoulos, A., 2013. Comparison of PV systems with maximum DC voltage 1000V and 1500V. In: Conference Record of the IEEE Photovoltaic Specialists Conference.

Guerrero-Lemus, R., Vega, R., Kim, T., Kimm, A., Shephard, L.E., 2016. Bifacial solar photovoltaics - A technology review. Renew. Sustain. Energy Rev..

Gul, M., Kotak, Y., Muneer, T., Ivanova, S., 2018. Enhancement of albedo for solar energy gain with particular emphasis on overcast skies. Energies.

Gupta, M.K., Bumtariya, K.J., Shukla, H.A., Patel, P., Khan, Z., 2017. Methods for evaluation of radiation view factor: A review. In: Materials Today: Proceedings.

Hamilton, D.C., Morgan, W.R., 1952. Radiant-interchange configuration factors. National Advisory Committee for Aeronautics.

Howell, J.R., Mengüç, M.P., Siegel, R., 2020. Thermal Radiation Heat Transfer, seventh ed. CRC Press.

Iqbal, M., 1983. An Introduction To Solar Radiation, 1st ed Elsevier.

Krysl, P., 2017. Finite Element Modeling with Abaqus and Python for Thermal and Stress Analysis, first ed. Pressure Cooker Press, San Diego.

Lam, S.K., Pitrou, A., Seibert, S., 2015. Numba: A LLVM-based python JIT compiler. In: Proc. Second Work. LLVM Compil. Infrastruct. HPC - LLVM '15.

Libal, Joris., Kopecek, Radovan., 2018. Bifacial photovoltaics: Technology, applications and economics, first ed. IET.

Mckay, D.C., 1985. Estimating solar irradiance on inclined surfaces: A review and assessment of methodologies. Int. J. Sol. Energy.

Middel, A., Lukasczyk, J., Maciejewski, R., Demuzere, M., Roth, M., 2018. Sky view factor footprints for urban climate modeling. Urban Clim..

Mirhosseini, M., Rezania, A., Rosendahl, L., 2017. View factor of solar chimneys by Monte Carlo method. In: Energy Procedia.

Muneer, T., Ivanova, S., Kotak, Y., Gul, M., 2015. Finite-element view-factor computations for radiant energy exchanges. J. Renew. Sustain. Energy.

Okereke, M., Keates, S., 2018. Finite element mesh generation. In: Springer Tracts in Mechanical Engineering.

Rammohan Rao, V., Sastri, V.M.K., 1996. Efficient evaluation of diffuse view factors for radiation. Int. J. Heat Mass Transfer.

Rehman, N.U., Siddiqui, M.A., 2015. A novel method for determining sky view factor for isotropic diffuse radiations for a collector in obstacles-free or urban sites. J. Renew. Sustain. Energy.

Sarmento, R., Costa, V., 2017. Comparative approaches to using R and Python for statistical data analysis.

Szabó, B., Babuška, I., 2011. Introduction To Finite Element Analysis: Formulation, Verification and Validation.